Energy 357 (2026) 140772

Contents lists available at ScienceDirect

Energy

journal homepage: www.elsevier.com/locate/energy

Investigating the dynamic possibilities of a nuclear sCO_2 power conversion cycle for naval implementation ☆

Tom H. Wien [a,b,*], Gert-Jan Meijn [c], Rene Pecnik [a], Jurriaan W.R. Peeters [a]

[a] Process & Energy – ME, Delft University of Technology, Delft, The Netherlands
[b] Royal Netherlands Navy, Den Helder, The Netherlands
[c] Research Development & Innovation, Damen Naval, Vlissingen, The Netherlands

ARTICLE INFO

Keywords:
Nuclear
Supercritical carbon dioxide
Power cycles
Modelling
Dynamics
Naval propulsion

ABSTRACT

This study assesses the technical feasibility of nuclear propulsion for naval vessels by investigating the dynamics of a Very High Temperature Reactor combined with a supercritical carbon dioxide recompression cycle. By applying a dynamic model that includes the reactor, heat exchangers, and turbomachinery, the power dynamics of a nuclear energy conversion system are compared with those of common prime movers on a naval vessel. Results show that the turbine bypass valve, in combination with the dump cooler, enables a power ramp of 90%/min. During this power ramp, the reactor temperature stays within safety limits and experiences temperature variations of less than 25 degrees, the shaft speed remains stable with deviations of less than 0.25% RPM, and turbomachinery performs within design limits regarding temperature, pressure ratio and mass flow rate. However, the current turbine bypass valve design, which maintains a stable reactor output, results in a low overall cycle efficiency at part load. Furthermore, temperature- and pressure gradients of up to ±1.48 °C/s and ±0.38 bar/s occur within the heat exchangers during the power transient, which could affect the integrity of the materials. Further research could focus on a design that limits the thermal integrity concerns within the heat exchanger, and could implement energy storage capabilities to optimize the waste heat of the cycle during part-load.

1. Introduction

There is currently a resurgence of interest in nuclear propulsion with the Dutch maritime sector aiming to develop a standardized, modular nuclear reactor for ship integration within 10 years [1]. Nuclear energy offers a carbon-free power source, supporting the decarbonization of the maritime sector, while also providing a significantly higher energy density than other (renewable) alternatives [2]. This high energy density power source is particularly beneficial for the volume limited space of a naval vessel. This way nuclear power generation also aids in coping with the increasing energy demands of rail-guns, high-power radars, and unmanned systems [3], while limiting the volume increase of the power generation system. Additionally, nuclear power offers significant operational advantages, as it extends operational duration with fewer logistical dependencies (e.g. refuelling at sea), while enabling naval vessels to respond more rapidly to crises, improving overall strategic autonomy [4]. Despite its historical use in naval applications [5,6], implementing nuclear power in future vessels presents significant challenges, especially for countries not already possessing this technology.

One of the possible technical implications for nuclear technology onboard of a naval vessel is the required power dynamics. Naval vessels experience significant fluctuations in power demand, with conventional prime movers like gas turbines achieving ramp rates of up to 90% per minute [7]. In contrast, nuclear reactors are designed for a stable power output, making it essential to evaluate their dynamic response for successful deployment in naval vessels.

Historically, the Pressurized Water Reactor (PWR) has been the most widely used type of reactor, accounting for 70% of all operational land-based reactors [8]. However, Generation IV reactor designs offer improved efficiency, safety, and economic viability [9,10]. Among these designs is the Very High Temperature Reactor (VHTR), which is designed specifically for producing heat at high outlet temperatures, with some designs reaching temperatures up to 1000 °C [9,10]. In addition, its technological development is relatively advanced compared to other Generation IV reactors, as its predecessor, the High-Temperature Gas-cooled Reactor (HTGR), has already been operated successfully [11].

☆ This article is part of a Special issue entitled: 'sCO2-2025' published in Energy.

* Corresponding author at: Process & Energy – ME, Delft University of Technology, Delft, The Netherlands.
E-mail address: Tom.H.Wien@gmail.com (T.H. Wien).

https://doi.org/10.1016/j.energy.2026.140772
Received 28 June 2025; Received in revised form 16 February 2026; Accepted 15 March 2026
Available online 11 May 2026

Within nuclear power plants, steam cycles are commonly used to convert the heat generated by the reactor to useful electricity [12]. However, the supercritical carbon dioxide (sCO_2) cycle provides a more efficient alternative. Above the critical point of CO_2 (30.98 °C and 7.38 MPa), the fluid enters a supercritical state characterized by gas-like diffusivity and liquid-like density [13]. This results in a higher cycle efficiency at elevated temperatures compared to a steam cycle [13–16]. In addition, the volume to power ratio of sCO_2 turbomachinery is lower than conventional steam turbines [13–16], providing a volume that is up to 10 times smaller than conventional turbomachinery [17]. This is especially of interest for a (naval) vessel where volume is already limited, making it the preferred cycle configuration for a VHTR placed on board a vessel.

To assess the power dynamics of a nuclear power plant, the VHTR in combination with the sCO_2 power conversion cycle was selected. Several studies have already explored (nuclear) sCO_2 cycles in different contexts. Dostal [13] investigated the feasibility and cycle configuration for a nuclear sCO_2 power conversion cycle, while Carstens [18] compared several control configurations for such a power cycle. Olumayegun and Wang [19] analysed the dynamics of a waste heat recovery sCO_2 cycle, and Ming et al. [20] investigated the transient behaviour of a nuclear reactor with a direct-driven sCO_2 cycle. The South Korean research institute KAIST has also assessed the potential of nuclear sCO_2 cycles for maritime applications, providing insights into cycle configurations and a transient analysis [21–24].

However, existing research lacks a detailed cycle design for maritime purposes, along with a dynamic performance comparison against a conventional naval propulsion system. In this paper, these gaps are addressed to determine the feasibility of nuclear propulsion as a viable alternative to fossil fuel-based propulsion systems in naval vessels.

2. Cycle design

Before designing the power conversion cycle, a suitable naval vessel is selected as a reference. Given the Royal Netherlands Navy's developments, the Future Air Defender (FuAD) project was identified as the most viable option. Set to replace the Air Defence and Command Frigates by 2034 [25], this vessel demands significant power for advanced weapons, sensors, and high-speed operations within a carrier strike group, making nuclear propulsion a compelling choice. In addition, the vessel demands high power dynamics for acceleration and manoeuvring, which was previously addressed by the implementation of gas turbines, capable to achieve ramp rates up to 90% per minute [7]. Accounting for modularity and the required redundancy of the power generation within the vessel, it was decided to design a nuclear power plant of 8 MW_e at Full Power (FP). Combining multiple smaller power plants into a multi-reactor setup ensures sufficient propulsion and hotel load power is provided to the vessel. Here, full electric propulsion was selected for its flexibility, volume efficiency, and potential integration of energy storage for propulsion. Lastly, to account for the global operation of a naval vessel, the seawater inlet temperature was set to 35 °C [26].

The nuclear reactor within the cycle produces heat, and to convert this heat to useful electricity for the hotel load and propulsion of the vessels, a power conversion cycle must be implemented. For this purpose, the indirect sCO_2 recompression cycle was selected. Among the various sCO_2 cycle designs, the indirect recompression cycle has a high efficiency, relatively simple design, and provides technological maturity [13,18,27]. The layout of the indirect recompression cycle is presented in Fig. 1 and an overview of the design parameters are presented in Tables 1 and 2. Within this cycle, a nuclear reactor (R) serves as the heat source, utilizing helium as the working medium in the primary circuit. To maintain sufficient pressure, a blower (B) is implemented into the primary circuit. Additionally, a dump cooler (DCL) is included, which can be activated by valve V5 to decrease the inlet temperature of the helium. The heat present within the helium will be transferred to the sCO_2 cycle by the intermediate heat exchanger (IHX). The sCO_2 cycle applies a single-stage turbine (T) and generator (G), but adds an additional compression stage, resulting in a main compressor (MC) and a re-compressor (RC). To optimize cycle efficiency, two recuperators, a low- and high temperature recuperator (LTR and HTR), are positioned after each compressor. A cooler (CL) transfers leftover heat from the cycle to the seawater. To ensure sufficient mass flow from the seawater is entering the coolers, two pumps (P) are added to the system. Finally, throttle valves (V1-V4) are implemented to maintain safe and stable cycle pressure, while a turbine bypass valve (V6) controls cycle power by controlling the mass flow through the turbine. The system's components are connected by pipes, which are disregarded in this research due to their expected negligible impact on the (dynamic) performance of the cycle [19].

Table 1
Design values of the power conversion cycle.

Parameter	Value
Working fluid	Supercritical carbon dioxide (sCO_2)
Cycle type	Indirect recompression
Turbomachinery type	Radial/centrifugal
Thermal power [MW_{th}]	20.0
Electrical power [MW_e]	7.9
Efficiency [%]	39.5
Cycle pressure [bar]	90–225
Cycle mass flow [kg/s]	114.78
Split ratio [-]	0.71
Seawater inlet temperature [°C]	35
Heat exchanger TTD [°C]	10

Table 2
Steady state power requirements per component.

Component	Value
Reactor	20.00 MW
Turbine	13.15 MW
Main compressor	2.96 MW
Re-compressor	2.13 MW
Generator	8.06 MW
Load	7.90 MW
Cooling	11.94 MW
Blower	0.36 MW

For this study the reactor design of the 10 MW_{th} U-battery was chosen, as its power output is within the range of the required power output, and a detailed design, required for model implementation, is publicly available [28–31]. The design of the U-battery is the most detailed for its 10 MW_{th} variant, but this is not sufficient for a power cycle of 8 MW_e, which requires a higher thermal power input. For this reason it was decided to implement two 10 MW_{th} reactors within each cycle, which are placed parallel to each other. These reactors will be controlled in similar fashion, thus providing 20 MW_{th} to the secondary cycle. The reactor uses helium to transfer the heat from the reactor core to the secondary cycle, which enters the reactor at a temperature of 400 °C and is heated up to 750 °C [28].

For the turbomachinery, radial sCO_2 turbomachinery were selected, as these are deemed more efficient at the relatively low power output of designed power conversion cycle [27]. A radial turbomachinery design similar to that proposed by Oh et al. [32] was selected as they present detailed performance maps of sCO_2 turbomachinery within the desired power output range. These designs apply a compression ratio of 2.5, an expansion ratio of 2.44, a compressor efficiency of 84.9% and a turbine efficiency of 91.9% [32]. To ensure operation above the critical point in the sCO_2 cycle, a lower cycle pressure of 90 bar was selected which results in a higher cycle pressure of 225 bar. This remains within common pressure levels of an sCO_2 cycle [19,27] and was therefore accepted. A turbine-alternator-compressor (TAC) configuration was chosen for its simplicity and technological maturity [27].

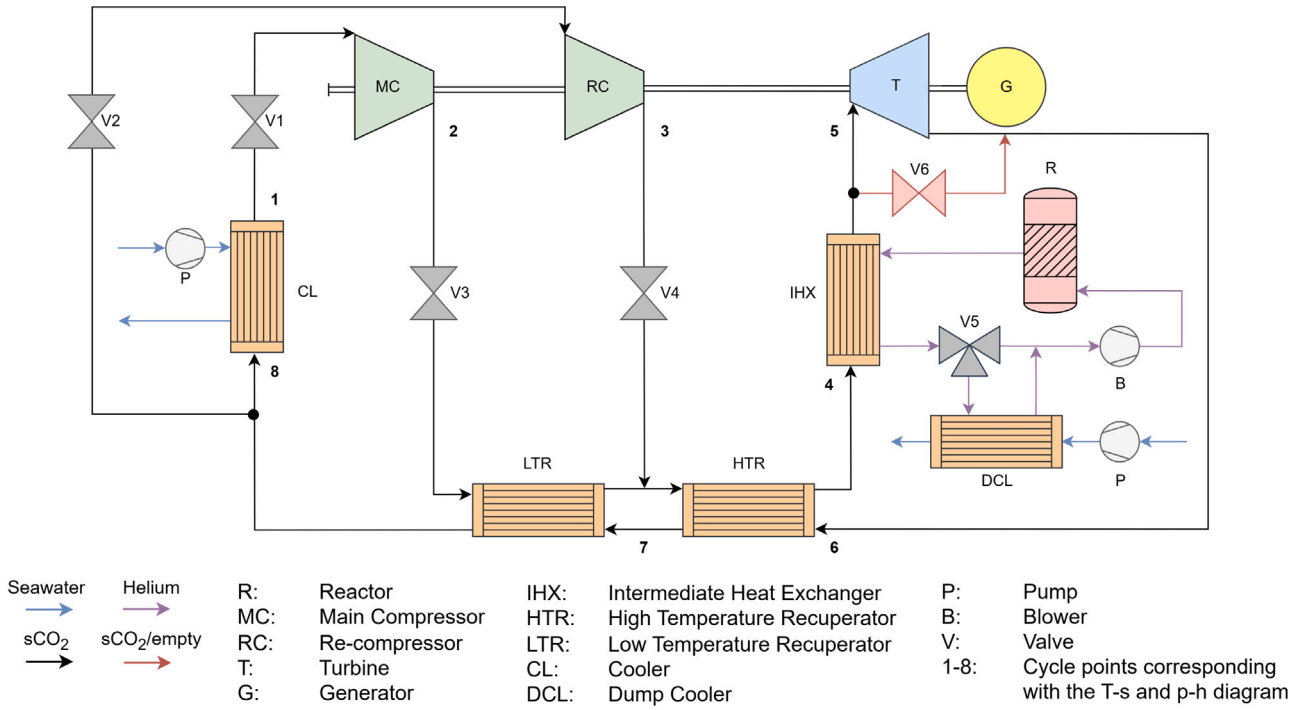

Fig. 1. Schematic overview of the designed nuclear sCO_2 recompression cycle.

The wavy-channelled Printed Circuit Heat Exchanger (PCHEs) was chosen for all heat exchangers within the cycle because of its enhanced heat transfer capabilities, compact size and ability to operate at the temperature and pressure levels used in this cycle [19,20,27,33,34]. The heat exchanger material is assumed to be Stainless Steel 316L, the material properties for which can be found in Appendix A.1. Here, the material properties used by Marchionni et al. [33] are applied, as their model is validated with experimental data. The sizing limits stated by Olumayegun et al. [34] are accounted for regarding height, width and length of the heat exchanger. Furthermore, the Terminal Temperature Difference (TTD) was set to 10 °C [19] and the flow regime is kept turbulent throughout the whole channel with an appropriate channel diameter. Finally, pressure losses within the channels must be kept low to ensure sufficient pressure at the lower cycle side. For an expansion ratio of 2.44, a higher cycle pressure of 225 bar corresponds to a lower cycle pressure of 92.2 bar. To maintain a sufficient lower cycle pressure, the total pressure drop across all sCO_2 heat exchangers was limited to 2 bar. An iterative approach was applied in which the channel length, channel diameter and number of channels within the heat exchangers were adjusted until the specified design constraints were met, of which Appendix A.1 provides the specific design parameters.

The conditions set in operating pressure and temperature enable a detailed design of the sCO_2 recompression cycle. Based on these conditions and system characteristics, the developed T-s and p-h diagrams of the cycle are presented in Figs. 2 and 3, illustrating the cycle points as defined in Fig. 1. Here, the principle is applied that if two thermodynamic properties are known, all other thermodynamic properties can be determined by CoolProp using a proper equation of state and thermophysical property correlations [35–37]. The design of the cycle does not account for potential pressure losses that occur within the heat exchanger, meaning that the pressure at each cycle point is equal to the higher or lower cycle pressure. The remaining thermodynamic properties are derived based on the heat exchanger TTD, turbomachinery efficiency (which determines outlet enthalpy), or the fixed heat input from the reactor. A step-by-step approach is presented in Appendix A.2. The design targets maximum power output by increasing the mass flow rate until an energy balance across the HTR is achieved at 114.78 kg/s. The compressor split fraction is set to

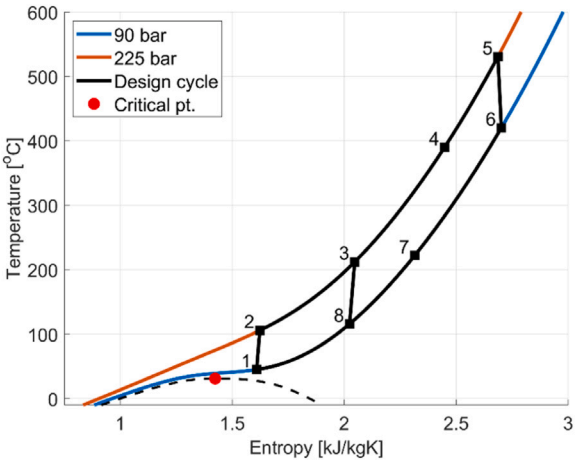

Fig. 2. T-s diagram of the sCO_2 cycle.

0.71 to satisfy the LTR energy balance. As a result, the turbine produces 13.15 MW and the main compressor and re-compressor consume 2.96 MW and 2.13 MW, respectively, which results in 8.06 MW being delivered to the generator. As the reactor delivers 20 MW_{th} of heat to the cycle, the result is a required cooling power of 11.94 MW.

To control the power dynamics, a preliminary investigation indicated that relying solely on reactor power control is unsatisfactory, as it led to slow overall power dynamics or unsafe temperature conditions within the reactor [38]. To address this issue, the reactor is operated at a constant power output and a dump cooler (DCL) was incorporated to regulate the reactor inlet temperature. However, this is a preliminary design solution, and further research can improve the location of the DCL, as its current location directly exposes it to potentially radioactive materials of the reactor. Bypass control is deemed the fastest control method [13,18] and as fast power dynamics are preferred this control method was implemented. The turbine bypass valve is the most commonly used bypass valve [18,32,39] and was therefore selected.

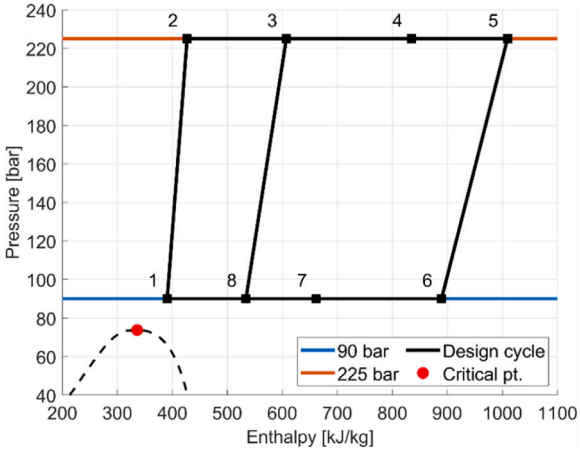

Fig. 3. P-h diagram of the sCO_2 cycle.

3. Modelling method

An overview of the model is presented in Fig. 4, which includes each component of the nuclear sCO_2 recompression cycle shown in Fig. 1. All the components are modelled using Simulink [40] in which the ordinary differential equation (ode) solver ode23tb (stiff/TR-BDF2) was selected, because it can handle stiff equations. For each component, the model solves relevant transport equations numerically, which will be discussed in the sections hereafter. Each thermodynamic state is characterized by a combination of mass flow, pressure, and enthalpy. The scope of this model is constrained to the naval vessel's switchboard as dynamic limitations of the propulsion system have been previously addressed by Wien and Meijn [38].

During the simulation of the power conversion cycle, several thermodynamic properties must be calculated. These properties can vary significantly, particularly for CO_2 operating near its critical point. To address this, CoolProp (f_{cp}) was applied to calculate thermodynamic properties based on the known values of at least two other properties. For example, the temperature T can be determined if the pressure p and enthalpy h are known, i.e.

$$T = f_{cp}(p, h). \tag{1}$$

For supercritical CO_2, the Span & Wagner 1996 equation of state and appropriate correlations for thermal conductivity and viscosity were employed [41–43]. Similarly, for water and helium, well-known thermophysical property data was used [44–49].

3.1. Reactor

To model the neutron kinetics of the nuclear reactor, the point kinetics equations (PKEs) were applied. In these equations spatial dependences are neglected, removing the spatial variation within the reactor [50]. As a result, neutron density varies solely with time, making this approach well-suited for preliminary dynamic power simulations. The point kinetics equations, in their six-group form, are given by [30,50,51]

$$\frac{dn}{dt} = \frac{\rho - \beta}{\Lambda} n + \sum_{j=1}^{6} \lambda_j c_j, \tag{2}$$

$$\frac{dc_j}{dt} = \frac{\beta_j}{\Lambda} n - \lambda_j c_j, \text{ with j} = 1,2,\ldots,6. \tag{3}$$

Here n represents the neutron population, which is directly related to the reactor's thermal power, ρ denotes the change in reactivity, β is the total effective delayed neutron fraction, Λ is the prompt neutron generation lifetime, λ refers to the effective decay constant and c is the concentration of a delayed neutron group [30]. Based on a reactor analysis performed with Serpent, Atkinson et al. [30] provide the required point kinetic parameters for the U-battery.

The reactivity within the model is dependent on the height of the control rods, and a thermal reactivity feedback mechanism, as given by

$$\rho = \rho_{rod} + \rho_{Tf} = \rho_{rod} + \alpha_{Tf}(T_f - T_{f,0}). \tag{4}$$

According to the relationship between rod height and reactivity, established by Atkinson et al. [30], the power output of the U-battery can be regulated by adjusting the height of the six control rods as

$$H_{rod} = H_{t_0} + v_{rod}\, t \rightarrow \rho_{rod} = f_{map}(H_{rod}). \tag{5}$$

Here the relation between reactivity and control height has been applied according to Fig. 5 and translates a given rod height to a change in reactivity. Atkinson et al. [31] state that if a single control rod is fully withdrawn at a constant speed of 120 s, a controlled and stable power increase is achieved. As the height of the rod itself is 1.6 m, this results in a rod velocity of 0.0133 m/s. As the simulation applies 6 control rods, it was decided to limit the rod speed during the simulation to a sixth of this value, thus $v_{rod,max} = \pm$ 0.0022 m/s. This limitation in control speed limits the dynamics of the reactor, but is of importance to ensure the reactor does not enter the prompt critical region. To maintain a symmetrical power distribution within the reactor core, all control rods are raised or lowered simultaneously. Furthermore, the reactivity changes based on a temperature difference of the fuel T_f compared to a reference fuel temperature $T_{f,0}$. As a result, the reactivity will lower when the temperature increases of the reactor, therefore ensuring an inherent safe reactor. For the U-battery, the negative feedback coefficient is equal to −4.26 pcm/K [30].

The heat generated within the fuel elements is transferred to the helium flowing through the reactor. The helium then transfers the heat generated by fission to the sCO_2 in the secondary circuit via the intermediate heat exchanger. However, the reactor comprises several components that affect the rate at which heat transfer occurs. An 1D thermal-hydraulics structure of the reactor can be used to represent the thermal inertia of the materials present within the reactor [31,51,52]. Fig. 6 provides an overview of the created thermal-hydraulics model, which is based on the material structure of the U-battery as described by Atkinson et al. [31]. Each reactor component is modelled through mass and energy conservation equations, which in its general form is given by [20,31,51,52]

$$M C_p \frac{dT}{dt} = \dot{Q} - U A \Delta T \tag{6}$$

Here, M represents the mass, C_p the specific heat capacity, T the temperature, $\dot{Q}$ the heat generated within the fuel elements (determined by the PKEs), U the overall heat transfer coefficient and A the heat transfer area between the materials. The specific equation for each component is presented in Appendix A.3. Within the reactor, heat transfer between components occurs primarily through conduction, while convection contributes to the overall heat transfer coefficient only through interactions with the flowing coolant. The thermal structure presented in Fig. 6 applied on the U-battery must account for the cylindrical structure of the reactor. The overall heat transfer coefficients and the heat transfer area of the different materials, are therefore calculated by [53]

$$\frac{1}{UA} = \frac{ln(r_{out}/r_{in})}{2\pi k H} + \frac{1}{2\pi r_{out} h H}. \tag{7}$$

The physical sizing of the cylinder is implemented by the outside and inside radius r and the height H according to dimensions of the U-battery provided by Atkinson et al. [31]. The convective heat transfer coefficient h was determined by applying the Gnielinski equation for the Nusselt number and the Petukhov relation for the friction factor. The thermal conductivity k and other material properties are presented in Appendix A.3.

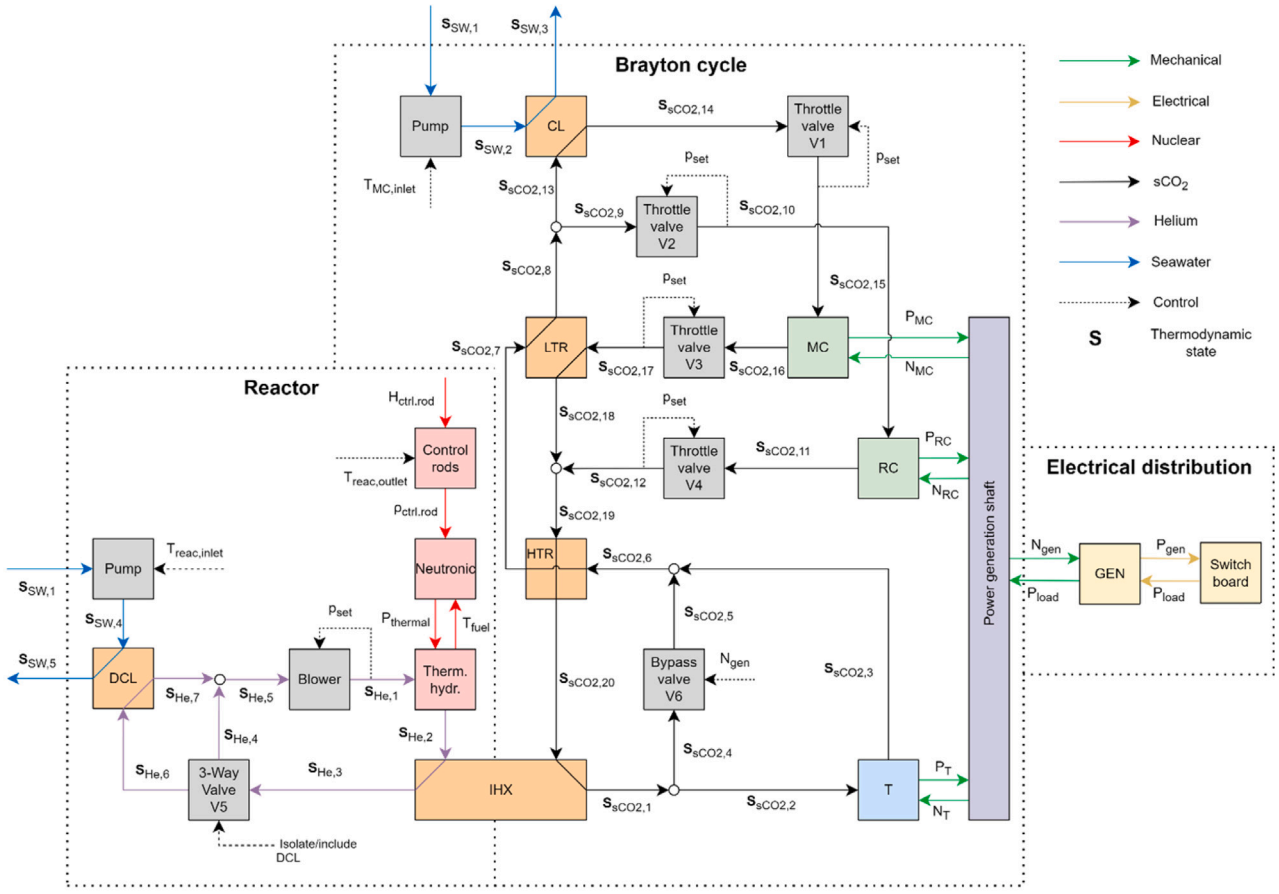

Fig. 4. Schematic overview of the dynamic model of the nuclear sCO_2 recompression cycle.

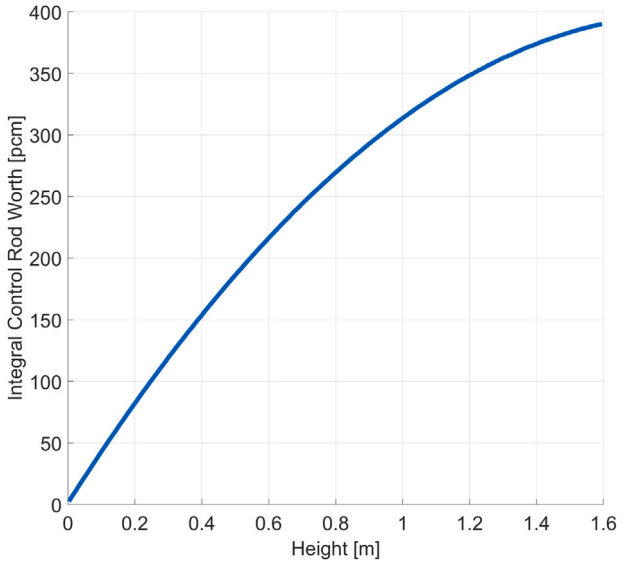

Fig. 5. Reactivity change and the control height within the U-battery [31].

The model also incorporates pressure losses within the coolant channels of the fuel blocks and the reflector. The pressure losses in these blocks have been calculated according to the pressure loss due to the height and the friction, as given by [20,54]

$$\Delta p = \rho g \Delta H + \frac{\rho f u^2 H}{2 d_H}. \tag{8}$$

Here, the flow density ρ, gravity constant g, the height of the channel H, the friction factor f, the flow speed u and the hydraulic diameter d_H are used to determine the pressure difference Δp that occurs over the channel. The pressure losses are mitigated by a blower, modelled by the method of Olumayegun et al. [34], thus ensuring a constant pressure of 40 bar within the primary circuit.

3.2. Heat exchangers

To accurately capture the thermal inertia of the heat exchangers within the system, a dynamic heat exchanger model is formulated. As presented in Fig. 7, the model of the heat exchanger is split into several nodes n along its length, applying a 1D finite volume method at each node. Each node contains two flow channels (one hot and one cold), which are counter flowing. The two channels are separated by the wall w of the heat exchanger [20,33]. A total of 20 nodes are used for each heat exchanger, as this results in an optimum regarding model accuracy and required simulation time. The mass and energy conservation equation is applied within each node for the hot h and cold c channels as given by [20]

$$M_h \frac{dh_h}{dt} = \dot{m}_{h,i}\, h_{h,i} - \dot{m}_{h,o}\, h_{h,o} - \dot{Q}_{hw,n}, \tag{9}$$

$$M_c \frac{dh_c}{dt} = \dot{m}_{c,i}\, h_{c,i} - \dot{m}_{c,o}\, h_{c,o} + \dot{Q}_{wc,n}. \tag{10}$$

Within these equations, M represents the mass of the fluid, $\dot{m}$ the mass flow rate, h the enthalpy and $\dot{Q}$ the heat transfer between the channel and the wall. The heat transfer is determined according to the overall heat transfer equation, as given by [20,53]

$$\dot{Q}_{hw,n} = U_{h,n} A_{h,n} (T_{h,n} - T_{w,n}), \tag{11}$$

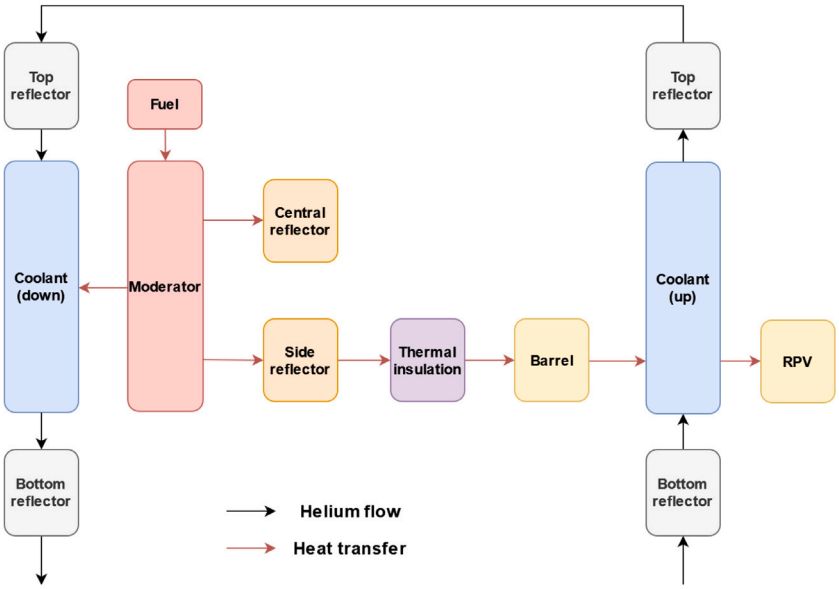

Fig. 6. Schematic diagram of the lumped thermal hydraulics of the reactor.

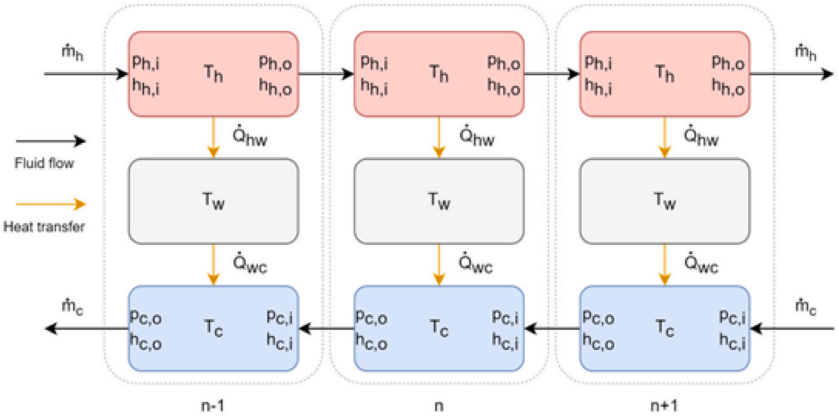

Fig. 7. Node division of the 1D heat exchanger model.

$$\dot{Q}_{wc,n} = U_{c,n} A_{c,n} (T_{w,n} - T_{c,n}). \tag{12}$$

The heat transfer depends on the overall heat transfer coefficient U, the heat transfer area A and the temperature T difference between the channels and the wall. Here, the fluid temperature within the heat transfer elements (T_h or T_c) is defined as the average of the inlet and outlet temperatures at each node. The wall temperature of the heat exchanger T_w is determined by applying the energy conservation equation to the wall w, as given by [20,53]

$$M_{w,n} C_{w,n} \frac{dT_{w,n}}{dt} = \dot{Q}_{hw,n} - \dot{Q}_{wc,n}. \tag{13}$$

Further more, to determine the overall heat transfer coefficient U the following equations have been applied on each node: [20,34,53]

$$\frac{1}{U} = \frac{1}{h_h} + \frac{t_e}{k_w} + \frac{1}{h_c}, \tag{14}$$

$$h = \frac{Nu\ k}{d_H}. \tag{15}$$

The thermal resistance of the wall is calculated by applying the equivalent plate thickness t_e and the thermal conductivity k of the wall. The convective thermal resistance of the hot and cold channel can be determined from the Nusselt number Nu. The Nusselt number itself is calculated according to the Gnielinski correlation, corrected for the wavy channel of the PCHE with the correction factors presented by Marchionni et al. [33]. The friction factor in the Gnielinski correlation is derived using Serghides' solution to the Colebrook–White equation [33]. For the equivalent plate thickness, the heat transfer area and the mass of the fluids and the wall, the method of Ming et al. [20] has been applied. The pressure drop along the heat exchanger channels is given by [20,34,54]

$$\Delta p_n = \frac{\rho_n f u_n^2 L_n}{2 d_H}. \tag{16}$$

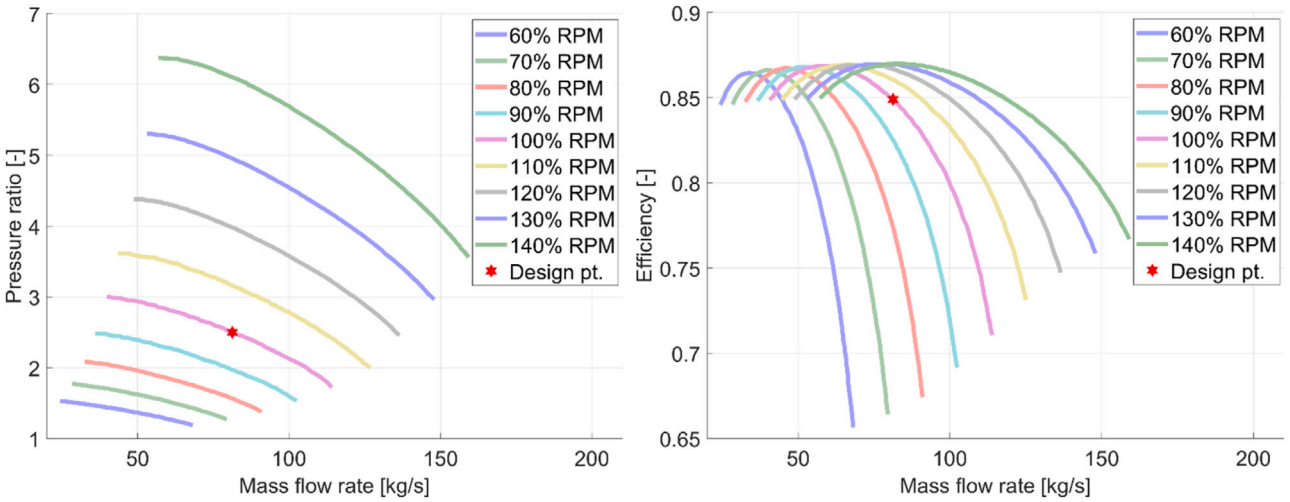

Fig. 8. Performance maps of the main compressor, normalized from the maps of Oh et al. [32].

Here, the pressure drop Δp depends on the density of the fluid ρ, the friction factor f, the flow velocity u, the length of the channel L and the hydraulic diameter d_H.

3.3. Turbomachinery

In dynamic power simulations, the response time of turbomachinery is often neglected, as the thermal dynamics of reactors and heat exchangers are significantly slower [27,39,55]. Therefore, the compressors and turbine are modelled by employing performance characteristic maps to determine the performance, the efficiency and pressure ratio, of the turbomachinery. Oh et al. [32] provide sCO_2 turbomachinery performance maps for a 12.5 MW_e nuclear sCO_2 power conversion cycle. By applying a normalization approach, these maps have been adapted for the 7.9 MW_e power conversion cycle, with the main compressor performance maps shown in Fig. 8 and the maps for the re-compressor and turbine in Appendix A.4.

Since these performance maps are generated based on specific inlet conditions (i.e. pressure and temperature), variations in operating conditions during dynamic simulations will affect turbomachinery performance [56,57]. To account for these differences, correction equations developed by Pham et al. [56] were implemented by the method of Alsawy et al. [57]. The correction equations by Pham et al. [56] account for changes in the isentropic exponent of CO_2, which are significant near its critical point [39,56]. As a result, the turbomachinery performance can be determined as follows: [57]

$$\pi = f_{map}(\dot{m}_{corr}, N_{corr}), \tag{17}$$

$$\eta = f_{map}(\dot{m}_{corr}, N_{corr}). \tag{18}$$

The corrected mass flow $\dot{m}_{corr}$ and the corrected shaft speed N_{corr} are used to determine the pressure ratio π and efficiency η of the turbomachinery. The pressure ratio is used to obtain the pressure at the outlet of the compressors C and turbine T, while the efficiency determines the enthalpy h as given by [27,57]

$$h_{C,o} = h_{C,i} + \frac{h_{C,o,isen} - h_{C,i}}{\eta_C}, \tag{19}$$

$$h_{T,o} = h_{T,i} - \eta_T(h_{T,i} - h_{T,o,isen}), \tag{20}$$

$$s = f_{cp}(h_i, p_i) \rightarrow h_{o,isen} = f_{cp}(s, p_o). \tag{21}$$

Here, the isentropic enthalpy h_{isen} uses the fact that for a reversible process entropy s is constant [57]. The total power P produced or consumed by the turbomachinery is determined through an energy balance over the system, as given by [34]

$$P_C = \dot{m}_C(h_{C,o} - h_{C,i}), \tag{22}$$

$$P_T = \dot{m}_T(h_{T,i} - h_{T,o}). \tag{23}$$

It is assumed that the generator does not impact the dynamic power behaviour of the power conversion and will only have an impact on the amount of power produced, which is accounted for by an overall generator efficiency η_{gen} set to 98.7% [34]. As a result, the electricity P_{elec} produced by the power conversion cycle can be calculated with a power balance of the turbine, compressors, pumps and blower, as given by [34]

$$P_{elec} = (P_T - \sum P_C)\eta_{gen} - \sum P_{P/B}. \tag{24}$$

3.4. Shaft model

For a recompression cycle applying a TAC configuration, the rotational speeds of the turbine, compressor and external load are similar. As a result, the shaft speed will only vary by a change in positive torque generated by the turbine or a negative torque produced by the compressors or external load [20]. The transient behaviour of the shaft is therefore calculated by [19,20,32]

$$I_{tot} N \frac{dN}{dt} = P_T - P_{MC} - P_{RC} - \frac{P_{load}}{\eta_{gen}}. \tag{25}$$

The dynamics of the shaft speed can be calculated according to the inertia I, the shaft speed N and the power P of the various components connected to the shaft. The electrical load demand is accounted for by assuming a constant generator efficiency, this way neglecting (electrical) dynamics of the generator. Pope [58] determined the shaft inertia for a 2400 MW_{th} nuclear sCO_2 recompression cycle. These inertia values were scaled down to match the conversion cycle as designed within this paper, based on the thermal power output of the nuclear reactors [32], of which the results have been presented in Table 3. The total shaft inertia is equal to the summation of the inertia of the individual machines and the shaft itself as given by

$$I_{tot} = I_T + I_{MC} + I_{RC} + I_G + I_{shaft}. \tag{26}$$

Table 3
Moment of inertia (kgm^2) by Pope [58] and for the scaled power conversion cycle.

Cycle power	Turbine	Main compressor	Recompressor	Generator	Shaft	Total
2400 MW_{th}	850	305.6	113.1	1000	186	2454.7
20 MW_{th}	7.08	2.55	0.94	8.33	1.55	20.46

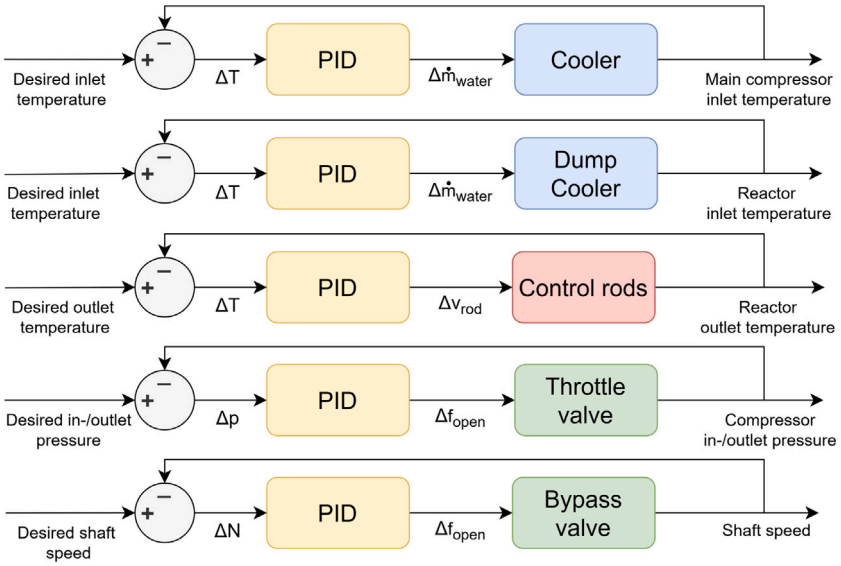

Fig. 9. Overview of the control methods applied within the model.

3.5. Control valves

The power conversion cycle contains several valves, which can be categorized as either throttle or bypass valves. Throttle valves are located just before and just after the compressors, typically experiencing low pressure differences. The supercritical state of CO_2 can be regarded as a single phase, and for valves with a small pressure difference, the orifice flow equation for liquid-like fluids can be used, as given by [39]

$$\dot{m} = C_v f_{open} \sqrt{2\rho(p_i - p_o)}. \tag{27}$$

A bypass valve is placed between the high and low pressure side of the power conversion cycle (i.e. in parallel with the turbine), experiencing large pressure differences. Therefore, the mathematical model for an orifice plate flow with large pressure differences is used for controlling the outlet pressure, i.e., [39]

$$\dot{m} = C_v f_{open} \left(\frac{2}{\gamma+1}\right)^{\frac{\gamma+1}{2(\gamma-1)}} \sqrt{\gamma \rho_i p_i}\ , \text{ for } \frac{p_o}{p_i} < \left(\frac{2}{\gamma+1}\right)^{\frac{\gamma}{\gamma-1}}, \tag{28}$$

$$\dot{m} = C_v f_{open} \sqrt{\frac{2\gamma}{\gamma-1}\rho_i p_i \left(\left(\frac{p_o}{p_i}\right)^{\frac{2}{\gamma}} - \left(\frac{p_o}{p_i}\right)^{\frac{\gamma+1}{\gamma}}\right)}\ , \text{ for } \left(\frac{2}{\gamma+1}\right)^{\frac{\gamma}{\gamma-1}} \leq \frac{p_o}{p_i} < 1. \tag{29}$$

These equations relate the mass flow $\dot{m}$ to a valve construction coefficient C_v, the relative opening area of the valve f_{open}, the flow density ρ, the pressure difference between the inlet p_i and outlet p_o of the valve, and the specific heat ratio γ [39]. Note that at these conditions the CO_2 can be considered an ideal gas.

4. Control

To achieve the dynamic power transients in the nuclear power plant, controllers must be integrated, of which an overview is presented in Figs. 4 and 9 and in Table 4. These controllers not only regulate the system's power output, but also ensure stable and safe operation. The control strategies are categorized into two groups: disturbance rejection and set-point tracking. Disturbance rejection includes control of the main compressor inlet temperature, reactor in-/outlet temperatures and compressor in/-outlet pressures, while set-point tracking only considers bypass valve control. Proportional-Integral-Derivative (PID) controllers are implemented to regulate parameters within the model.

4.1. Disturbance rejection control

The physical properties of CO_2 near its critical point change significantly and to make sure the main compressor operates within a stable region the inlet conditions must be controlled. The inlet temperature of the main compressor is controlled at 45 °C by adjusting the amount of seawater passing through the cooler [39]. This control method was not deemed necessary for the re-compressor as it operates at a temperature further away from the critical point. Additionally, the inlet pressure of the compressors is managed at 90 bar using throttle valves (V1 & V2). These valves ensure that the pressure does not exceed the designed lower cycle pressure, if sufficient inlet pressure is available. Throttle valves are also placed at the end of both compressors (V3 & V4). Here, the valve after the main compressor (V3) prevents the cycle pressure exceeding the 250 bar limit [19]. The valve after the re-compressor (V4) ensures that the outlet pressure of the re-compressor matches the outlet pressure of the LTR, preventing flow reversal damaging the turbomachinery [18].

Disturbance rejection is also applied to the reactor to ensure stable operation. A preliminary study [38] determined that reactor dynamics are too slow to meet the rapid power demands of a naval vessel. As a result, the reactor is operated constantly at full power, minimizing its disturbances to the overall system dynamics. Although the reactor is designed for stable operation, it remains important to actively control the reactor and keep it within a stable operating region, as otherwise

Table 4
Overview of the applied controllers.

Controlled system	Controlled value	Controlled parameter	Desired value
Cooler	$\Delta\dot{m}_{water}$	Inlet temp. main compressor	45 °C
Dump Cooler	$\Delta\dot{m}_{water}$	Inlet temp. reactor	400 °C
Control rods	Δv_{rod}	Outlet temp. reactor	750 °C
Throttle valve (V1-V2)	Δf_{open}	Inlet pres. compressors	<90 bar
Throttle valve (V3)	Δf_{open}	Outlet pres. main compressor	<250 bar
Throttle valve (V4)	Δf_{open}	Outlet pres. re-compressor	Outlet pres. LTR
Bypass valve (V6)	Δf_{open}	Shaft speed	100% RPM

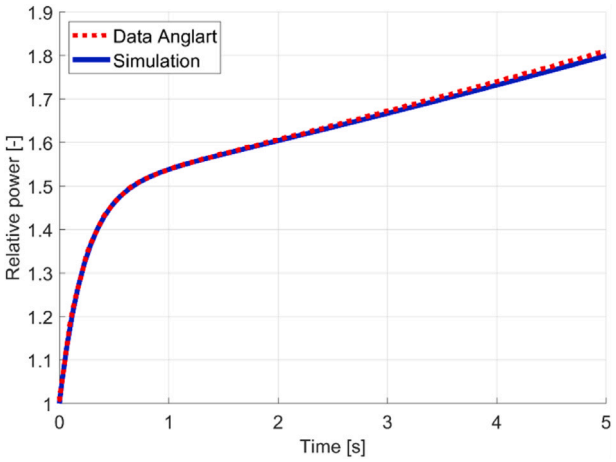

Fig. 10. Validation results of the point kinetics model, compared to Anglart [59].

material temperatures could exceed safety limits [30,38]. To achieve this, the reactor outlet temperature is regulated at 750 °C by adjusting the speed of the control rods, while the inlet temperature is maintained at 400 °C by adjusting the amount of seawater passing through the DCL and activating the three-way valve (V5). Both controllers ensure that the temperature does not increase or decrease by more than 25 °C, this protecting the materials within the reactor [30].

4.2. Set-point tracking control

Since the reactor operates at a constant power output, only one set-point tracking control method is applied in this study: the turbine bypass valve (V6). This valve controls the amount of mass flow entering the turbine by adjusting its opening. Because mass flow is directly related to the turbine's power output, as presented in Eq. (23), the bypass valve regulates the power output of the turbine and the overall cycle. As the power demand of the vessels changes, a torque imbalance will result in a change of shaft speed according to Eq. (25). By regulating the turbine power output, the bypass valve stabilizes the shaft speed and maintains it at the desired operating point of 100% RPM.

5. Validation

Each component of the dynamic model has been validated according to literature. First, the point kinetics equations were validated against literature data of Anglart [59], of which the results are shown in Fig. 10. Only a small deviation is visible, which can be explained by rounding of numbers within the presented numbers by Anglart [59]. Atkinson et al. [30] provide the required point kinetic parameters for the U-battery, making the point kinetics model suitable for implementation. The thermal hydraulics of the reactor have been validated according to steady state temperature values of the U-battery [28–31], the results of which are presented in Table 5. The material temperatures reported by Atkinson et al. [28] differ slightly from those obtained in this study. The latter could be due to differences in the method used to select wall temperatures versus average material temperatures, as Atkinson et al. [28] do not specify which approach was applied. A large temperature gradient within a material could cause significant errors if wall and average temperatures are not distinguished. Furthermore, some temperatures reported by Atkinson et al. [28] are identical, which contradicts Fourier's law of thermal conduction. This suggests that the errors may arise from inaccuracies in the specification of the temperature location.

The heat exchanger model has been validated against Marchionni et al. [33], who presented experimental data of a sCO_2 PCHE. Figs. 11 and 12 present the development of the temperature and pressure over time at the outlet of the cold side of the PCHE compared to validation data. A small deviation can be observed during the steady state part of the simulation, especially for the temperature of the CO_2. The error is the largest at the end of the simulation, as the temperature deviates here by ±1.2%. This error could be explained by some missing material property values used by Marchionni et al. [33], which were therefore assumed equal to standard stainless steel 316L property values. In addition, the modelling method of Marchionni et al. [33] and the current method are similar, but not identical, which could also impact the validation results. The overall magnitude of the deviations is considered acceptable for this research. Therefore, the heat exchanger model is deemed validated for the preliminary dynamic assessment of a nuclear sCO_2 power conversion cycle.

For the modelling of the turbomachinery model, a steady state modelling method was selected, applying performance maps based on the sCO_2 turbomachinery of Oh et al. [32]. To validate the turbomachinery model, input values presented by Oh et al. [32] are used, while applying the non-altered turbomachinery performance maps of Oh et al. [32] for the compressor and the turbine. The validation results for the outlet pressure, temperature and produced or consumed power are presented in Table 6. Here, the model produces errors up to ±0.73%, which was deemed small enough and acceptable for the purpose of this research. Adapting the performance maps to different power outputs and operating conditions introduces additional uncertainty in their application. However, as the results will show, the turbomachinery operates well within the bounds of these maps, and this uncertainty is therefore not expected to significantly affect the overall results of this research.

6. Results

To determine whether the designed nuclear sCO_2 power conversion cycle can achieve the same ramp rate as current prime movers of a naval vessel, a dynamic power simulation was performed at the ramp rate of a gas turbine [7]. The simulation applies a ramp rate equal to 90%/min between base load (10% FP) and full load (100% FP), which is visible in Fig. 13. At 500 s, the simulation increases the load from 10% FP to 100% FP within 60 s. The load then remains constant at 100% FP for 1000 s, to ensure all the systems reach a steady state, before decreasing the power demand back to 10% FP within 60 s. This will indicate the operational conditions the cycle must withstand to achieve the maximum expected power ramp, and if the components within the cycle operate within a safe region throughout the transient.

Table 5
Steady state temperature comparison of the U-battery.

Material	Fuel	Matrix	Reflector	Insulation	Barrel	RPV
Atkinson et al. [28]	1023.15 K	1023.15 K	973.15 K	973.5 K	673.5 K	673.5 K
Model	1131.4 K	1127.5 K	1111.7 K	896.2 K	688.3 K	674.2 K
Error	10.58%	10.20%	14.24%	−7.94%	2.20%	0.10%

Table 6
Validation results for the created compressor and turbine model.

Output parameter	Compressor			Turbine		
	Oh et al. [32]	Model	Error	Oh et al. [32]	Model	Error
Pressure	20.000 MPa	20.005 MPa	0.03%	8.161 MPa	8.176 MPa	0.18%
Temperature	142.196 °C	142.236 °C	0.03%	440.752 °C	441.257 °C	0.11%
Power	9.340 MW	9.372 MW	0.34%	21.750 MW	21.592 MW	−0.73%

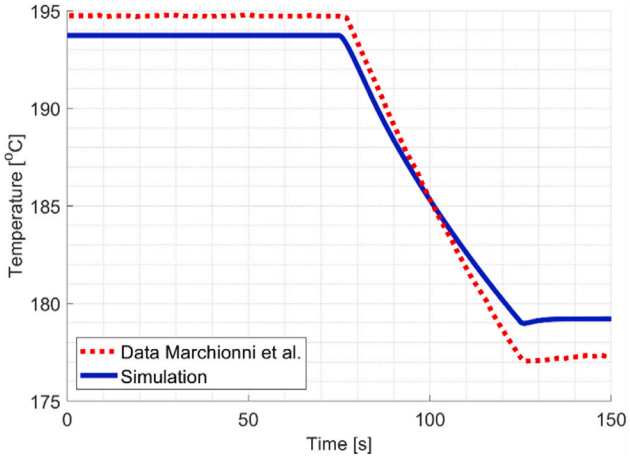

Fig. 11. Temperature development at the outlet of the cold side of the PCHE, compared to Marchionni et al. [33].

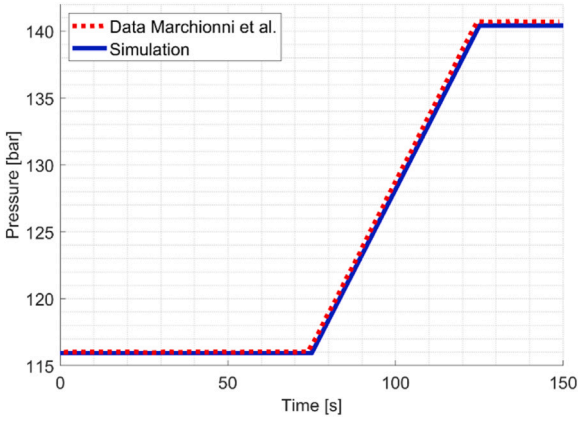

Fig. 12. Pressure development at the outlet of the cold side of the PCHE, compared to Marchionni et al. [33].

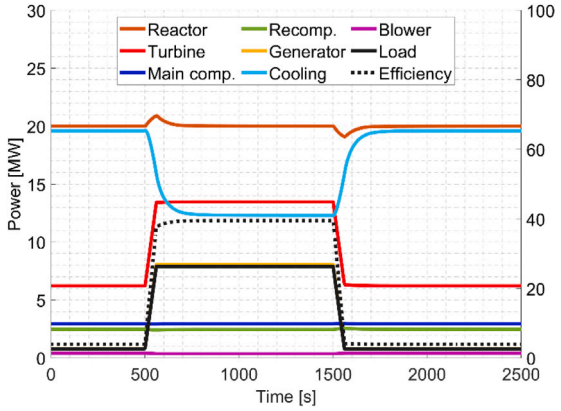

Fig. 13. Cycle efficiency and power production/ consumption of different cycle components.

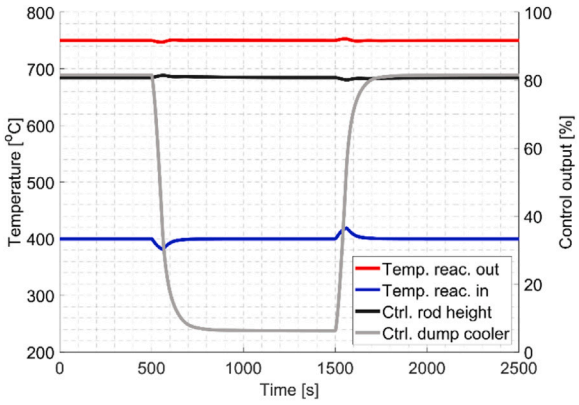

Fig. 14. In-/outlet temperature of the reactor, and the corresponding control response.

The power balance over all the components, and the cycle efficiency, are presented within Fig. 13. It shows that the reactor has a stable power output at 20 MW throughout the power transient, ensuring that slower reactor dynamics do not impact overall cycle dynamics. Fig. 14 shows that the outlet temperature is controlled by raising/lowering the control rods, while the inlet temperature is stabilized by the DCL. The results show that the change of the in-/outlet temperature of the reactor stays within the safety margin of 25 °C [30]. However, this operation requires excessive cooling power through the DCL at part-load, leading to a significant reduction in overall cycle efficiency as shown in Fig. 13, but results in a safe operating reactor. A higher cycle efficiency can be ensured by adding thermal or electrical energy storage capabilities in new designs, or by improving the control configuration or strategy.

As the load increases at 500 s, the power of the turbine increases to stabilize the shaft speed. This is realized by the turbine bypass valve,

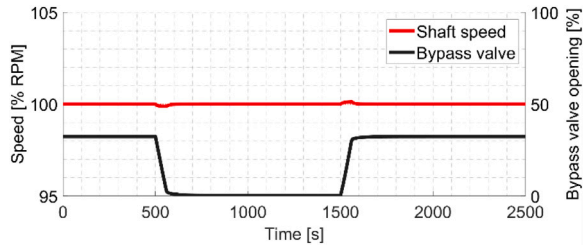

Fig. 15. Shaft speed and bypass valve opening during the power transient.

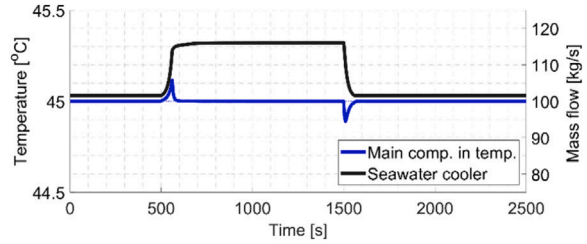

Fig. 16. Main compressor inlet temperature and water mass flow through the cooler.

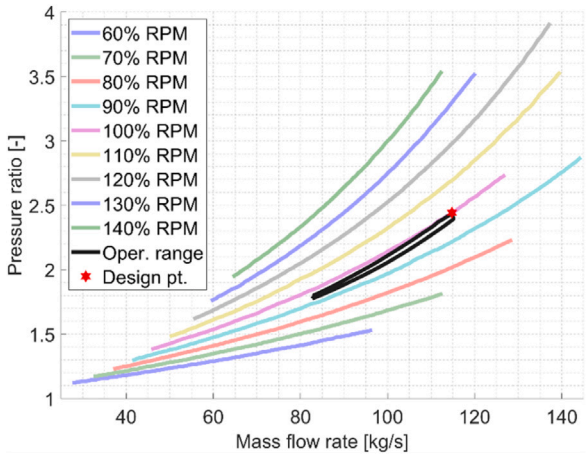

Fig. 17. Turbine performance map including the performance during the transient.

which closes at 500 s as visible in Fig. 15. As the load decreases at 1500 s, the turbine bypass valve opens to decrease the turbines power output to match the power demand. Fig. 13 shows that the power of the compressors stays relatively stable; by correcting the power output of the turbine, the shaft speed is kept stable, with a deviation smaller than 0.25% RPM.

During the power transient, the bypass valve changes the mass flow rate of the turbine, which impacts the turbine as shown in the performance map in Fig. 17. The expansion ratio decreases when the valve is opened, but the turbine stays within a safe region as it does not enter choke or surge areas. Fig. 18 shows that at part load, the turbine's temperature is higher than at full load. This is the result of waste heat recirculating through the bypass valve and the HTR, increasing the temperature of the sCO_2 before it enters the IHX. Since the reactor operates continuously at full power, this preheated sCO_2 increases in temperature. Furthermore, the reduced expansion ratio at part load raises the turbine's outlet pressure, as shown in Fig. 19, increasing the temperature even further. Still, the temperature remains within an acceptable range for sCO_2 turbomachinery [27], and the turbine is therefore considered to operate within a safe region.

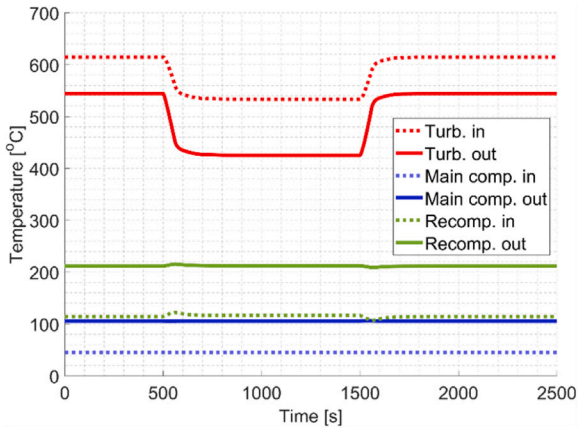

Fig. 18. Temperature development of the turbomachinery during the power transient.

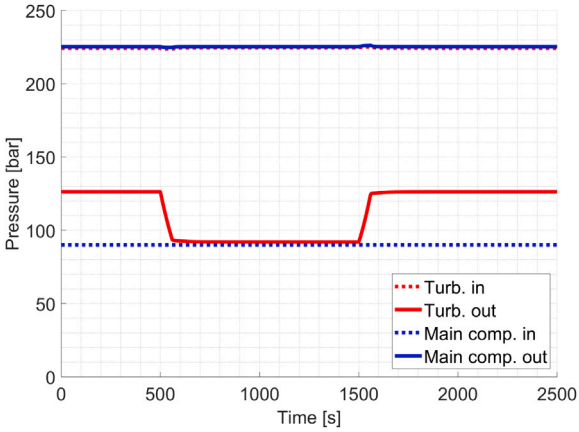

Fig. 19. Pressure development of the turbomachinery during the power transient.

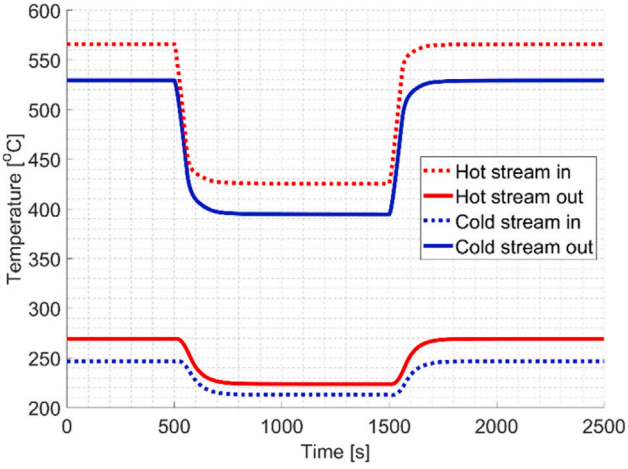

Fig. 20. Temperature development of the HTR.

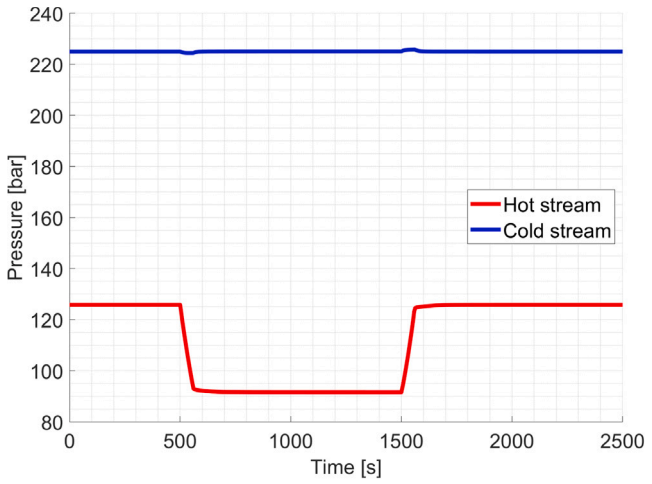

Fig. 21. Pressure development of the HTR.

Since the main compressor operates near the critical point of CO_2, it is important to control the inlet conditions for maintaining stable compressor performance. The main compressor inlet temperature is regulated by adjusting the mass flow through the cooler, as shown in Fig. 16. As the re-compressor operates further from the critical point of CO_2, no temperature control was applied, which explains the small temperature deviations within Fig. 18. Furthermore, Fig. 17 shows that during the transient, the turbine expansion ratio does not exceed its design value to ensure that the turbine outlet pressure is always higher than the compressor inlet pressure, see Fig. 19. This ensures that the system-wide pressure does not decrease. As the expansion ratio stays below the design value, the throttle valves are able to keep the inlet pressure of the compressors at 90 bar. The stable inlet temperature and pressure ensure that the compressors do not significantly perform outside of their design points and were therefore deemed safe throughout the power transient.

The PCHEs within the cycle endure varying operating temperatures and pressures throughout the power transient. They must not only withstand maximum temperatures of up to 750 °C (reactor outlet temperature) and pressures of up to 225 bar (highest sCO_2 cycle pressure), but also endure significant temperature and pressure gradients during the power transient. The largest gradients are observed within the HTR, for which the temperature and pressure development is presented within Figs. 20 and 21. During the transient, temperature gradients reach up to ±1.48 °C/s, while pressure gradients reach up to ±0.38 bar/s. Current material standards for PCHEs do not clearly define the limitations for temperature and pressure levels, as well as their gradients, making it uncertain whether standard PCHE designs can reliably withstand these conditions. Further research should define safety limits for the PCHE, to indicate if the current gradients would compromise reliability.

7. Conclusion

This study investigates whether combining a high-temperature reactor with an sCO_2 power conversion cycle can meet the transient power demands of a naval vessel. The nuclear sCO_2 recompression cycle designed in this work utilizes a turbine bypass valve as the control configuration, while the reactor remains a stable power source during the power transient with a ramp rate of 90%/min. The developed numerical model (including the nuclear reactor, heat exchangers, turbomachinery and control configuration) indicates that power dynamics similar to those of a gas turbine are feasible. It was shown that during transient operation, the reactor temperature does not vary significantly, turbomachinery operates within its performance region and that the shaft speed remains stable as well.

During the power transient, operating conditions within the Printed Circuit Heat Exchangers (PCHEs) reach temperature and pressure gradients up to ±1.48 °C/s and ±0.38 bar/s. It is unclear if these gradients could result in a violation of safety standards. Therefore, it is recommended that further research be focused on investigating the effect of transients in relation to material and safety limits. Additionally, the nuclear sCO_2 recompression cycle can be improved by including a form of energy storage as this will lead to better utilization of reactor heat than the current system does.

CRediT authorship contribution statement

Tom H. Wien: Writing – original draft, Validation, Software, Methodology, Investigation, Data curation, Conceptualization. **Gert-Jan Meijn:** Writing – review & editing, Supervision, Methodology. **Rene Pecnik:** Writing – review & editing, Supervision, Methodology. **Jurriaan W.R. Peeters:** Writing – review & editing, Supervision, Methodology.

Declaration of competing interest

The authors declare that they have no known competing financial interests or personal relationships that could have appeared to influence the work reported in this paper.

Appendix. Section

A.1. Heat exchanger design

A design was selected through an iterative process of varying the length, channel diameter, and number of channels, resulting in the desired output conditions with acceptable mass channel flows and pressure losses. The specifics of this heat exchanger design are presented in Tables A.1 and A.2. The lower channel diameter of the IHX, while ensuring turbulent flow, results in a significantly higher pressure drop across the channel than in the other heat exchangers. Although the sCO_2 pressure drop is 0.56 bar, the lower pressure drop in the other heat exchangers results in a total cycle pressure drop of 1.92 bar, which complies with the previously mentioned 2.2 bar and was therefore deemed acceptable.

A.2. Design of the T-s and p-h diagram

To calculate each operating point, only two thermophysical properties must be known, as CoolProp is capable to determine each other required property. The number of the operating points relate to the cycle points presented in Fig. 1. To determine the thermophysical properties of each operating point (P), the following steps are applied:

Table A.1
General heat exchanger values.

Parameter	Value
Material	Stainless steel 316 L [33]
Density [kg/m^3]	8000 [60]
Specific heat capacity [J/kgK]	500 [60]
Thermal conductivity [W/mK]	15 [60]
Width wall [mm]	0.75 [61]
Plate thickness [mm]	1.8 [61]
Channel surface roughness	neglected [33]

Table A.2
Printed circuit heat exchanger design values.

Parameter	IHX	HTR	LTR	CL
Heat transfer duty [MW]	20.00	26.17	14.68	11.48
Fluid, hot/cold side [-]	He/sCO_2	sCO_2/sCO_2	sCO_2/sCO_2	sCO_2/Water
Mass flow, hot/cold side [kg/s]	11.01/114.78	114.78/114.78	114.78/81.28	81.28/108.83
Channel diameter [mm]	1.40	2.00	2.00	2.00
Module width [mm]	899	899	899	899
Module height [mm]	495	810	639	603
Module length [mm]	400	1450	1460	990
Volume [m^3]	0.178	1.056	0.839	0.537
Number of channels per row [-]	418	327	327	327
Number of rows [-]	275	450	355	335
Hot side inlet/outlet temp. [°C]	750/400	420/222	222/116	116/45
Cold side inlet/outlet temp. [°C]	390/531	212/390	105/212	35/55
Hot/cold side pressure loss [kPa]	72.86/56.69	48.60/17.28	49.78/8.95	10.42/8.22
Hot/cold side channel flow [g/s]	0.096/0.99	0.78/0.78	0.99/0.70	0.74/0.99

Table A.3
Properties of the materials within the U-battery.

Reactor part	Specific heat capacity [J/kgK]	Thermal conductivity [W/mK]	Density [kg/m^3]
Fuel element	1473 [62]	65.4 [62]	1650 [62]
Central reflector	720 [28]	133 [28]	1800 [28]
Matrix layer	720	133	1750 [29]
Side reflector	720 [28]	133 [28]	1800 [28]
Thermal insulation	1200 [63]	0.23 [64]	3200 [29]
Barrel	557 [65]	19.8 [65]	8000 [29]
RPV	557 [65]	19.8 [65]	8000 [29]

1. The lower and higher cycle pressure are known, which results that at least one thermophysical property is known for each design point.
2. A water temperature of 35 °C, and a TTD of 10 °C results in a temperature of 45 °C at P1.
3. The efficiency of the main compressor, and the enthalpy at point 1, determine the enthalpy at P2.
4. The temperature at the outlet of the LTR should be 10 °C higher than P2, resulting in the temperature at P8.
5. The efficiency of the recompressor, and the enthalpy at P8, determine the enthalpy in P3.
6. The temperature at the inlet of the LTR should be 10 °C higher than P3, resulting in the temperature at P7.
7. The reactor inlet temperature of 400 °C, and a TTD of 10 °C result in the temperature at P4.
8. P5 and P6 are limited by the overall mass flow of the system. Maximum mass flow is desirable, resulting in more power in the turbine, but there are two limitations. First, the heat of the reactor is limited to 20 MW_{th}, limiting the amount of heat entering the secondary cycle. The temperature of P5 is therefore related to the cycle mass flow, as a higher mass flow would result in a lower temperature in P5. As the turbine characteristic is set, the temperature in P6 is directly influenced by the conditions in P5. If the temperature in P6 should account for the TTD with P4, this means P5 must have a known temperature (and thus limited mass flow) so that the TTD between P4 and P6 is satisfied. Secondly, the HTR provides the temperature increase from P3 to P4 due to leftover heat provided by the enthalpy change between P6 and P7. If P6 would drop lower due to an increased cycle flow, then the enthalpy difference between P6 and P7 could drop below the enthalpy difference between P3 and P4, realizing P4 cannot be achieved by the recuperator. To satisfy both conditions, the model calculates the maximum mass flow in which both conditions are still valid and thus determines the temperature in P5 and thus P6.
9. The split ratio has an influence on the total cycle efficiency. To ensure optimal cycle efficiency, the difference in heat over the LTR should be set to 0, as then all the heat available is effectively transferred. The enthalpy difference between P2-3 and P7-8 should therefore be compensated in different mass flows. The split ratio is determined such that the total amount of energy at both sides is equal.

Applying these steps ensures that the thermophysical properties of each point in the power conversion cycle are known. This results in the T-s and p-h diagram of the designed cycle, which are presented in Figs. 2 and 3. Furthermore, the cycle mass flow was determined equal to 114.78 kg/s and the split ratio was set to 0.71.

A.3. Reactor model

For the lumped thermal hydraulics, each reactor component is modelled through mass and energy conservation equations. For the fuel (F), moderator (M), central reflector (CR), side reflector (SR), insulation (I), barrel (B), reactor pressure vessel (RPV), riser (Ri) and downcomer (Do), the equations are given by

$$M_F C_{p,F} \frac{dT_F}{dt} = \dot{Q} - U_{F,M} A_{F,M} (T_F - T_M), \tag{A.1}$$

$$M_M C_{p,M} \frac{dT_M}{dt} = U_{F,M} A_{F,M} (T_F - T_M) - U_{M,R} A_{M,R} (T_M - T_R) - U_{M,Do} A_{M,Do} (T_M - T_{Do}), \tag{A.2}$$

$$M_{CR} C_{p,CR} \frac{dT_{CR}}{dt} = U_{M,CR} A_{M,CR} (T_M - T_{CR}), \tag{A.3}$$

$$M_{SR} C_{p,SR} \frac{dT_{SR}}{dt} = U_{M,SR} A_{M,SR} (T_M - T_{SR}) - U_{SR,I} A_{SR,I} (T_{SR} - T_I), \tag{A.4}$$

$$M_I C_{p,I} \frac{dT_I}{dt} = U_{R,I} A_{R,I} (T_R - T_I) - U_{I,B} A_{I,B} (T_I - T_B), \tag{A.5}$$

$$M_B C_{p,B} \frac{dT_B}{dt} = U_{I,B} A_{I,B} (T_I - T_B) - U_{B,Ri} A_{B,Ri} (T_B - T_{Ri}), \tag{A.6}$$

$$M_{RPV} C_{p,RPV} \frac{dT_{RPV}}{dt} = U_{Ri,RPV} A_{Ri,RPV} (T_{Ri} - T_{RPV}), \tag{A.7}$$

$$M_{Ri} C_{p,Ri} \frac{dT_{Ri}}{dt} = U_{B,Ri} A_{B,Ri} (T_B - T_{Ri}) - U_{Ri,RPV} A_{Ri,RPV} (T_{Ri} - T_{RPV}) + \dot{m}_{in} h_{in} - \dot{m}_{out} h_{out}, \tag{A.8}$$

$$M_{Do} C_{p,Do} \frac{dT_{Do}}{dt} = U_{M,Do} A_{M,Do} (T_M - T_{Do}) + \dot{m}_{in} h_{in} - \dot{m}_{out} h_{out}. \tag{A.9}$$

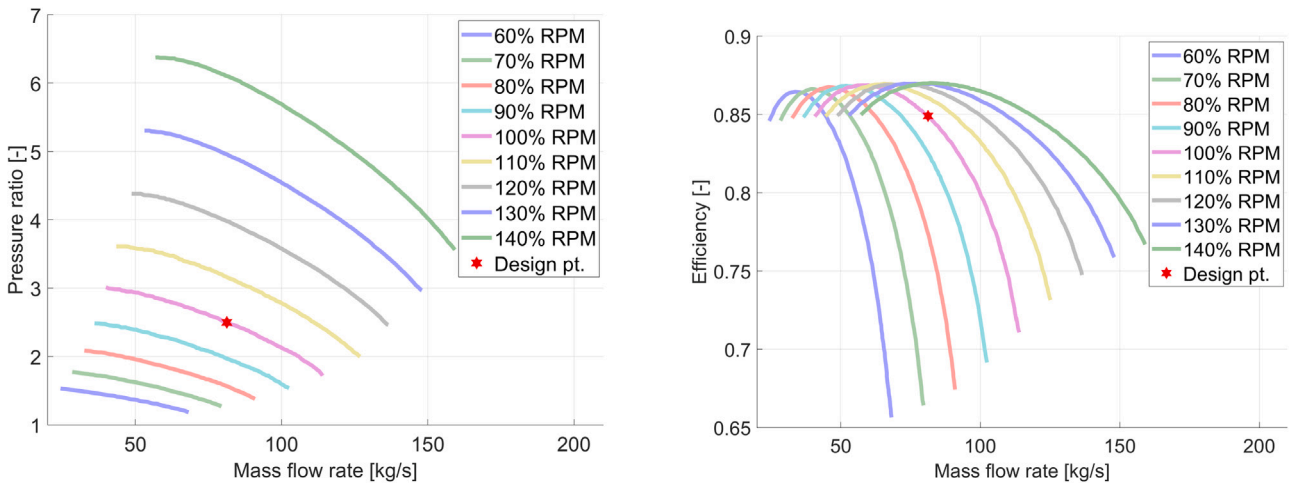

Fig. A.1. Main compressor performance maps.

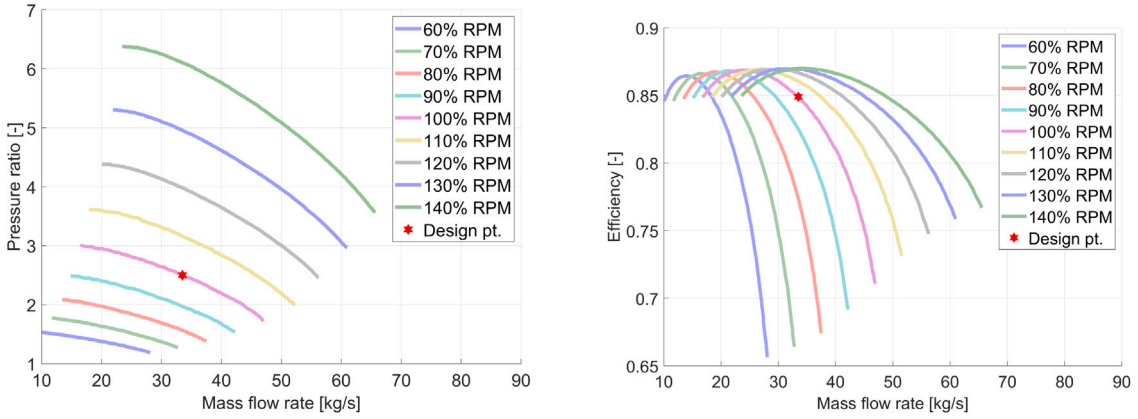

Fig. A.2. Re-compressor performance maps.

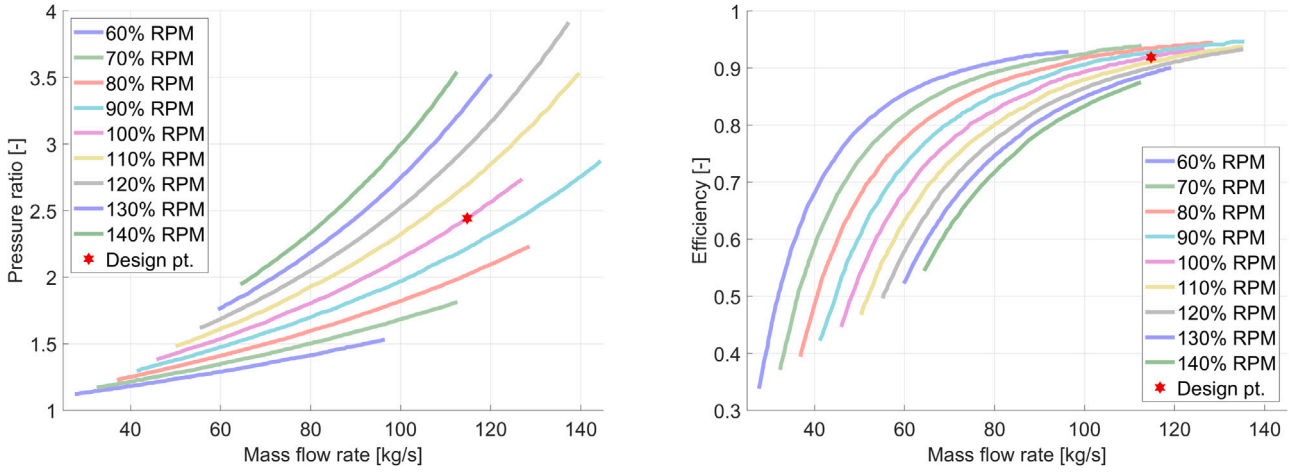

Fig. A.3. Turbine performance maps.

In addition, the material properties that have been used for these components are presented in Table A.3. As the material type of the matrix could not be specified, it is assumed it has a specific heat capacity and thermal conductivity comparable to the reflector. Further research could indicate the specific materials used within the reactor, and improve the material properties used within the model.

A.4. Turbomachinery

Based on the performance maps of Oh et al. [32] the performance maps for the turbomachinery have been generated, which are presentend in Figs. A.1–A.3.

Data availability

No data was used for the research described in the article.

References

[1] Dutch maritime sector. No guts, no Hollands Glorie!. 2023, https://www.rijksoverheid.nl/documenten/rapporten/2023/10/26/sectoragenda-mmi. [Accessed 21 March 2024].

[2] Van Zalk J, Behrens P. The spatial extent of renewable and non-renewable power generation: A review and meta-analysis of power densities and their application in the U.S.. Energy Policy 2018;123:83–91. http://dx.doi.org/10.1016/j.enpol.2018.08.023.

[3] Royal Netherlands Navy. Sail plan Vooruit!. 2023, https://www.rijksoverheid.nl/documenten/brochures/2023/05/17/brochure-sail-plan. [Accessed 21 March 2024].

[4] US Department of the Navy and Department of Energy. The United States naval nuclear propulsion program. 2015, https://shorturl.at/VWQU6. [Accessed 21 March 2024].

[5] Wang Q, Zhang H, Zhu P. Using nuclear energy for maritime decarbonization and related environmental challenges: Existing regulatory shortcomings and improvements. Int J Env Res Public Health 2023. http://dx.doi.org/10.3390/ijerph20042993.

[6] Freire LO, De Andrade DA. Historic survey on nuclear merchant ships. Nucl Eng Des 2015;293. http://dx.doi.org/10.1016/j.nucengdes.2015.07.031.

[7] General Electric. LM2500 aeroderivative gas turbine. 2024, https://www.gevernova.com/content/dam/gepower-new/global/en_{US}/downloads/gas-new-site/products/gas-turbines/lm2500-fact-sheet-product-specifications.pdf. [Accessed 21 March 2024].

[8] World nuclear association. World nuclear performance report 2023. 2023, https://www.world-nuclear.org/world-nuclear-performance-report.aspx. [Accessed 21 March 2024].

[9] Zohuri B. Generation IV nuclear reactors. Nucl React Technol Dev Util 2020;213–46. http://dx.doi.org/10.1016/B978-0-12-818483-7.00006-8.

[10] IAEA. Small modular reactors: Advances in SMR developments 2024. 2024, https://www.iaea.org/publications/{15790}/small-modular-reactors-advances-in-smr-developments-2024. [Accessed 12 February 2025].

[11] Nagatsuka K, Noguchi H, Nagasumi S, Nomoto Y, Shimizu A, Sato H, Nishihara T, Sakaba N. Current status of high temperature gas-cooled reactor development in Japan. Nucl Eng Des 2024;425:113338. http://dx.doi.org/10.1016/j.nucengdes.2024.113338.

[12] Tanum T. Advances in steam turbines for modern power plants. 2nd ed. Woodhead Publishing, LLC; 2022.

[13] Dostal V. A supercritical carbon dioxide cycle for next generation nuclear reactors [Ph.D. thesis], Massachusetts Institute of Technology; 2004.

[14] Choi S, Son IW, Lee JI. Comparative performance evaluation of gas Brayton cycle for micro–nuclear reactors. Energies 2023;16(4):2065. http://dx.doi.org/10.3390/en16042065.

[15] Wu P, Ma Y, Gao C, Liu W, Shan J, Huang Y, Wang J, Zhang D, Ran X. A review of research and development of supercritical carbon dioxide Brayton cycle technology in nuclear engineering applications. Nucl Eng Des 2020;368:110767. http://dx.doi.org/10.1016/j.nucengdes.2020.110767.

[16] Kissick SM, Wang H. A comparative study of alternative power cycles for small modular reactors. Energy Convers Manage 2021;247:114734. http://dx.doi.org/10.1016/j.enconman.2021.114734.

[17] Ming Y, Tian R, Zhao F, Luo C, Tan S. Control strategies and transient characteristics of a $5MW_{th}$ small modular supercritical co2 Brayton-cycle reactor system. Appl Therm Eng 2023;235:121302. http://dx.doi.org/10.1016/j.applthermaleng.2023.121302.

[18] Carstens NA. Control strategies for supercritical carbon dioxide power conversion systems [Ph.D. thesis], Massachusetts Institute of Technology; 2007.

[19] Olumayegun O, Wang M. Dynamic modelling and control of supercritical co2 power cycle using waste heat from industrial processes. Fuel 2019;249:89–102. http://dx.doi.org/10.1016/j.fuel.2019.03.078.

[20] Ming Y, Liu K, Zhao F, Fang H, Tan S, Tian R. Dynamic modeling and validation of the 5 MW small modular supercritical CO2 Brayton-cycle reactor system. Energy Convers Manage 2022;253. http://dx.doi.org/10.1016/j.enconman.2021.115184.

[21] Son IW, Heo JY, Oh BS, Lee JI. Transient response of supercritical CO2 axial turbine for KAIST MMR. In: 3rd European supercritical CO2 conference. 2019, http://dx.doi.org/10.17185/duepublico/48896.

[22] Oh BS, Lee JI. Control schemes of S-CO2 cooled KAIST micro modular reactor as marine propulsion engine to treat rapid load change condition. 2019.

[23] Oh BS, Kim Y, Kim SJ, Lee JI. SMART with trans-critical CO2 power conversion system for maritime propulsion in Northern Sea Route, part 1: System design. Ann Nucl Energy 2020;149:107792. http://dx.doi.org/10.1016/j.anucene.2020.107792.

[24] Oh BS, Kim SJ, Kim Y, Lee JI. SMART with trans-critical CO2 power conversion system for maritime propulsion in Northern Sea Route, part 2: Transient analysis. Ann Nucl Energy 2021;150:107875. http://dx.doi.org/10.1016/j.anucene.2020.107875.

[25] Marineschepennl. Overzicht toekomstige nederlandse marineschepen. 2023, https://marineschepen.nl/dossiers/nieuwe-marineschepen-Nederland.html. [Accessed 21 March 2024].

[26] Seatemperatureorg. World sea temperatures. 2024, https://www.seatemperature.org/. [Accessed 26 June 2024].

[27] Brun K, Friedman P, Dennis R. Fundamentals and applications of supercritical carbon dioxide (SCO2) based power cycles. Woodhead Publishing; 2017.

[28] Atkinson S, Abram TJ, Litskevich D, Merk B. Small modular high temperature reactor optimisation– part 1: A comparison between beryllium oxide and nuclear graphite in a small scale high temperature reactor. Prog Nucl Energy 2019;111:223–32. http://dx.doi.org/10.1016/j.pnucene.2018.10.017.

[29] Atkinson S, Litskevich D, Merk B. Small modular high temperature reactor optimisation part 2: Reactivity control for prismatic core high temperature small modular reactor, including fixed burnable poisons, spectrum hardening and control rods. Prog Nucl Energy 2019;111:233–42. http://dx.doi.org/10.1016/j.pnucene.2018.11.001.

[30] Atkinson S, Aoki T, Litskevich D, Merk B, Xing Y. Part 3: Evaluating a small modular high temperature reactor design during control rod withdrawal and a depressurised loss of coolant accidents. Prog Nucl Energy 2021;134:103689. http://dx.doi.org/10.1016/j.pnucene.2021.103689.

[31] Atkinson S, Aoki T. The development of a fuel lifecycle reactivity control strategy for a generic micro high temperature reactor. Nucl Eng Technol 2024;56:785–92. http://dx.doi.org/10.1016/j.net.2023.07.022.

[32] Oh BS, Lee JI, Kim SG, Cho SK, Yu H. Transient analyses of s-co2 cooled kaist micro modular reactor with gamma+ code. In: The 11th international topical meeting on nuclear reactor thermal hydraulics, operation and safety Gyeongju. 2016.

[33] Marchionni M, Chai L, Bianchi G, Tassou SA. Numerical modelling and transient analysis of a printed circuit heat exchanger used as recuperator for supercritical co2 heat to power conversion systems. Appl Therm Eng 2019;161:114190. http://dx.doi.org/10.1016/j.applthermaleng.2019.114190.

[34] Olumayegun O, Wang M, Kelsall G. Thermodynamic analysis and preliminary design of closed Brayton cycle using nitrogen as working fluid and coupled to small modular sodium-cooled fast reactor (sm-sfr). Appl Energy 2017;191:436–53. http://dx.doi.org/10.1016/j.apenergy.2017.01.099.

[35] Span R, Wagner W. A new equation of state for carbon dioxide covering the fluid region from the triple-point temperature to 1100 K at pressures up to 800 MPa. J Phys Chem Ref Data 1996;25:1509–96. http://dx.doi.org/10.1063/1.555991.

[36] Huber ML, Sykioti EA, Assael MJ, Perkins RA. Reference correlation of the thermal conductivity of carbon dioxide from the triple point to 1100 K and up to 200 MPa. J Phys Chem Ref Data 2016;45:013102. http://dx.doi.org/10.1063/1.4940892.

[37] Laesecke A, Muzny CD. Reference correlation for the viscosity of carbon dioxide. J Phys Chem Ref Data 2017;46. http://dx.doi.org/10.1063/1.4977429.

[38] Wien TH, Meijn GJ. Dynamic potential of naval nuclear power generation: modelling of a high-temperature reactor with a supercritical carbon dioxide power conversion cycle. Institute of Marine Engineering, Science and Technology (IMarEST), http://dx.doi.org/10.24868/11209.

[39] Bian X, Wang X, Wang R, Cai J, Tian H, Shu G, Lin Z, Yu X, Shi L. A comprehensive evaluation of the effect of different control valves on the dynamic performance of a recompression supercritical CO2 Brayton cycle. Energy 2022;248:123630. http://dx.doi.org/10.1016/j.energy.2022.123630.

[40] The MathWorks, Inc. Simulink. Natick, Massachusetts, United States; R2024a. Available: https://www.mathworks.com/products/simulink.html.

[41] Span R, Wagner W. A new equation of state for carbon dioxide covering the fluid region from the triple point temperature to 1100 K at pressures up to 800 MPa. J Phys Chem Ref Data 1996;25:1509–96. http://dx.doi.org/10.1063/1.555991.

[42] Huber ML, Sykioti EA, Assael MJ, Perkins RA. Reference correlation of the thermal conductivity of carbon dioxide from the triple point to 1100 k and up to 200 MPa. J Phys Chem Ref Data 1996;25:013102. http://dx.doi.org/10.1063/1.4940892.

[43] Laesecke A, Muzny CD. Reference correlation for the viscosity of carbon dioxide. J Phys Chem Ref Data 2017;25:013107. http://dx.doi.org/10.1063/1.4977429.

[44] Ortiz-Vega DO, Hall KR, Holste JC, Arp VD, Harvey AH, Lemmon EW. Equation of state for helium-4. 2019, Unpublished; coefficients from REPROP10 used with permission.

[45] Hands BA, Arp VD. A correlation of thermal conductivity data for helium. Cryogenics 1981;21(12):697–703. http://dx.doi.org/10.1016/0011-2275(81)90211-3.

[46] Arp VD, McCarty RD, Friend DG. Thermophysical properties of Helium-4 from 0.8 to 1500 K with pressures to 2000 MPa. National Institute of Standards and Technology; 1998, NIST Technical Note 1334 (revised).

[47] Wagner W, Pruß A. The IAPWS formulation 1995 for the thermodynamic properties of ordinary water substance for general and scientific use. J Phys Chem Ref Data 2002;31:387–535. http://dx.doi.org/10.1063/1.1461829.

[48] Huber ML, Perkins RA, Friend DG, Sengers JV, Assael MJ, Metaxa IN, Miyagawa K, Hellmann R, Vogel E. New international formulation for the thermal conductivity of H_2O. J Phys Chem Ref Data 2012;41(3):033102. http://dx.doi.org/10.1063/1.4738955.

[49] Huber ML, Perkins RA, Laesecke A, Friend DG, Sengers JV, Assael MJ, Metaxa IN, Vogel E, Mare R, Miyagawa K. New international formulation for the viscosity of H_2O. J Phys Chem Ref Data 2009;38(2):101–25. http://dx.doi.org/10.1063/1.3088050.

[50] Duderstadt JJ, Hamilton LJ. Nuclear reactor analysis. John Wiley & Sons; 1976.

[51] Haipeng L, Huang X, Zhang L. A simplified mathematical dynamic model of the HTR-10 high temperature gas-cooled reactor with control system design purposes. Ann Nucl Energy 2008;35-9:1642–51. http://dx.doi.org/10.1016/j.anucene.2008.02.012.

[52] Dong Z, Pan Y. A lumped-parameter dynamical model of a nuclear heating reactor cogeneration plant. Energy 2018;145:638–56. http://dx.doi.org/10.1016/j.energy.2017.12.153.

[53] Mills AF, Coimbra CFM. Basic heat and mass transfer. 3rd ed. Temporal Publishing, LLC; 2015.

[54] Furlong AJ, Ge H, Hughes RW, Macchi A, Haelssig JB. Dynamic modelling of cross-flow printed circuit heat exchangers for multistage reactor intercooling. Appl Therm Eng 2024;239:122010. http://dx.doi.org/10.1016/j.applthermaleng.2023.122010.

[55] Wang X, Wang R, Bian X, Cai J, Tian H, Shu G, Li X, Qin Z. Review of dynamic performance and control strategy of supercritical CO2 Brayton cycle. Energy AI 2021;5:100078. http://dx.doi.org/10.1016/j.egyai.2021.100078.

[56] Pham HS, Alpy N, Ferrasse JH, Boutin O, Tothill M, Quenaut J, Gastaldi O, Cadiou T, Saez M. An approach for establishing the performance maps of the sc-co2 compressor: Development and qualification by means of cfd simulations. Int J Heat Fluid Flow 2016;61:379–94. http://dx.doi.org/10.1016/j.ijheatfluidflow.2016.05.017.

[57] Alsawy T, Mohammed RH, Mesalhy O, Elsayed ML. Dynamic performance of supercritical co2 bray ton cycle and its relationship to the correction of turbomachinery performance maps: A comparative analysis. Appl Therm Eng 2024;242:122364. http://dx.doi.org/10.1016/j.applthermaleng.2024.122364.

[58] Pope MA. Thermal hydraulic design of a 2400 MW_{th} direct supercritical CO2 cooled fast reactor [Ph.D. thesis], Massachusetts Institute of Technology; 2006.

[59] Anglart H. Nuclear reactor dynamics and stability. 2011.

[60] Thyssenkrupp. Stainless steel 316L 1.4404. 2024, https://www.thyssenkrupp-materials.co.uk/stainless-steel-316l-14404.html. [Accessed on: 27 June 24].

[61] Bennett K, Chen Y. Printed circuit heat exchanger performance analysis using non-uniform segmental design method. Appl Therm Eng 2019;153:69–84.

[62] Travis BW, El-Genk MS. Thermal–hydraulics analyses for 1/6 prismatic vhtr core and fuel element with and without bypass flow. Energy Convers Manage 2013;67:325–41.

[63] National Institute of Standards and Technology. Silicon carbide. 2024, https://webbook.nist.gov/cgi/cbook.cgi?ID=C409212&Units=SI&Type=JANAFS&Plot=on#JANAFS. [Accessed on: 24 September 2024].

[64] Atkinson Seddon. Design variances and optimisation of the u-battery [Ph.D. thesis], University of Sheffield; 2018.

[65] The Engineering Toolbox. Fluid flow - Hydraulic diameter. 2024, https://www.engineeringtoolbox.com/hydraulic-equivalent-diameter-d_458.html. [Accessed on: 05 October 2024].